Half-metallic porphyrin-based molecular junctions for spintronic applications

Azar Ostovan [1,*] Nick Papior,[2] and S. Shahab Naghavi[1,†]

[1]*Department of Physical and Computational Chemistry, Shahid Beheshti University, 1983969411 Tehran, Iran*
[2]*DTU Computing Center, Department of Applied Mathematics and Computer Science,*
Technical University of Denmark, DK-2800 Kongens Lyngby, Denmark

Single molecular magnets (SMMs) have become promising paradigms to develop novel spintronics for futuristic information technologies such as high-density information and quantum computing. The efficiency and characteristics of SMM devices are determined by the intrinsic nature of the molecular magnets placed in the spin transport pathway. In this work, to understand the role of the central magnetic ion on the performance of SMM devices, we screen the spin-conductance properties of whole $3d$ and $4d$ metalloporphyrins using the nonequilibrium Green's function formalism in conjunction with density functional theory. Our results show that the investigated SMMs according to spintronic conductance behavior can be categorized into three groups: type I non-spin-polarized, type II′ minor spin-polarized current, and type II″ major spin-polarized current devices. Type-II′ and type-II″ molecular systems show perfect spin filtering and spin-dependent negative differential resistance. The optimal energy alignment of spin-polarized molecular orbitals with gold electrodes results in one-channel spin transport (minor for type II′ and major for type II″). Thus type-II junctions are half-metal. The type-II″ junctions also show a voltage-induced spin switchability at low bias voltages. In this regard, type-II molecular systems are promising candidates for a low-power consumption spin filter, spin switch, memory, to name just a few. Our results highlight the practical applications of metalloporphyrin for the development of multipurpose miniature spintronic devices.

I. INTRODUCTION

Molecular spintronics, in which a single molecule behaves as a single magnet, has emerged as a revolutionary platform in nanoscale electronic circuits from both fundamental and technological perspectives [1,2]. They host various electronic systems such as spin-negative differential resistance (SNDR) [3], spin crossover (SCO) [4], spin filtering [5], and inversion of the spin polarization [6], to name a few.

In this context, single-molecule magnets (SMMs) that combine the advantage of magnetic molecule with bulk materials look like promising candidates for developing high-end electronic applications such as high-capacity data storage [7], magnetic sensing [8], and also because of their long electron-spin-relaxation time [9], for quantum computers [10]. Single-molecule magnets have a shapely defined electronic state and can be chemically tailored with atomic precision. Therefore, unique functionalities—with no classical analog—can be found in SMMs. Light and field switchability is one such example [7,11]. The SMMs' structure comprises an inner magnetic core surrounded by organic ligand(s) that link SMMs into a junction. The SMMs' spintronic efficiency depends on several key parameters such as contact geometry, the molecular end groups, and the nature of the molecules [12]. Therefore, understanding how

these factors are interrelated helps in the precise tailoring of SMMs for technological applications. Here the term "nature of molecule" comprises both the molecular chemistry and its central metal ion. Of course the metal ion—as the magnetic core of SMM—plays a crucial role in regulating the transport properties of target devices in the absence of an external magnetic field.

Among the studied molecular magnets, metal porphyrins (*M*Pors where *M* is a transition metal) as a building block of SMMs [13–15], offer a variety of desirable features such as highly conjugated structure, rigid and planar framework, and chemical and structural flexibility [16,17]. For example, an array of one-dimensional chromium porphyrin [14] shows half-metallic behavior suitable for spintronics applications. A study by Kuang *et al.* reveals that spin crossover can be controlled in FePor [13], at the single-molecule level. Though numerous in number, previous studies on metalloporphyrins have focused on a few systems to explore their spintronics efficiency. Thus a systematic and comprehensive screening to find a correlation between the magnetic core and spin properties of the built device is missing here.

Motivated by the excellent spin characteristics of metalloporphyrin and the lack of a systematic search, in the present work, we screen *M*Pors-based single molecules for $M = 3d$ and $4d$ transition metals for spintronic applications using high-throughput density functional theory (DFT) in conjunction with nonequilibrium Green's function (NEGF) formalism. We investigate the spin-resolved conductance properties of *M*Pors molecules ($M = 3d$ and $4d$ transition

---

*a_ostovan@sbu.ac.ir
†s_naghavi@sbu.ac.ir

metals) attached to the gold electrodes. Our results show that *M*Por-based molecular junctions under small voltage biases show a pure spin current and a spin-dependent negative differential resistance. Interestingly, some of the SMMs represent spin-state switchability upon applying voltage. It worth noting that almost all the studied *M*Por candidates have been synthesized and widely used for catalyst [18], sensor [19], and dye-sensitized solar cell [20] applications.

II. COMPUTATIONAL METHODS

DFT calculations: All density functional theory (DFT) calculations are performed using the generalized gradient approximation of Perdew-Burke-Ernzerhof (PBE) [21] as implemented in the SIESTA [22] software package. Throughout this work we used a double-ζ plus polarization (DZP) basis set with the Troullier-Martins norm-conserving pseudopotentials [23]. The cutoff energy was set to 500 eV to ensure the convergence of total energy. The structures are fully relaxed until forces on each atom become smaller than 0.02 eV Å^{-1}. The DFT method with U correction (DFT+U [24]) method was used to account for the on-site Coulomb interactions and localization of d electrons, which is the best we can do for such large devices. The optimum value of U for 3d and 4d transition metals are obtained from Jain *et al.*'s work [25] which are quite similar to reported values in another database [26].

The choice of pseudopotentials and Hubbard U could affect the accuracy of spin-transport calculations. To ensure the accuracy and reproducibility of the adopted method, we compare some of the calculated results with the previous experimental and theoretical work. As seen in the Supplemental Material (SM) Table S1 [46], our calculated spin magnetic moments for Mn, Fe, Ru, and Rh are, respectively, 5.03, 2.26, 2.24, and 0.92 μ_B, showing an excellent agreement with experimental [27–34] and computational works based on hybrid functionals [35–45] (see third and fourth columns of Table S1 [46]).

In our screening process we also considered Zn(II) and Cd(II) porphyrins which have, of course, no practical interest in spintronics. However, they provide valuable data that serve to find systematic trends. See the Supplemental Material for more details [46].

Transport calculations: The spin-dependent electron transport phenomena of *M*Por-based junctions are calculated with the NEGF formalism as implemented in TranSIESTA code [47], and using the model system shown in Figs. 1(a) and 1(b). The model device is divided into three regions: (1) the left electrode, (2) the central extended scattering region, and (3) the right electrode.

Electrode nanowires are composed of two relaxed gold (Au) unit cells. Each has constructed two sublayers of 3 and 7 Au atoms where the seven atom face mimics the Au (111) surface (Fig. S1 of the SM [46]). The nanowire Au electrodes were successfully used for the simulation of different conductance characteristics in nanoscale devices [48,49]. We tested various Au layers to ensure electron tunneling between the electrodes are avoided (see Fig. S2 (SM) [46]). The rest of the calculations are based on the extended scattering length at which the transmission coefficients converged. We find that
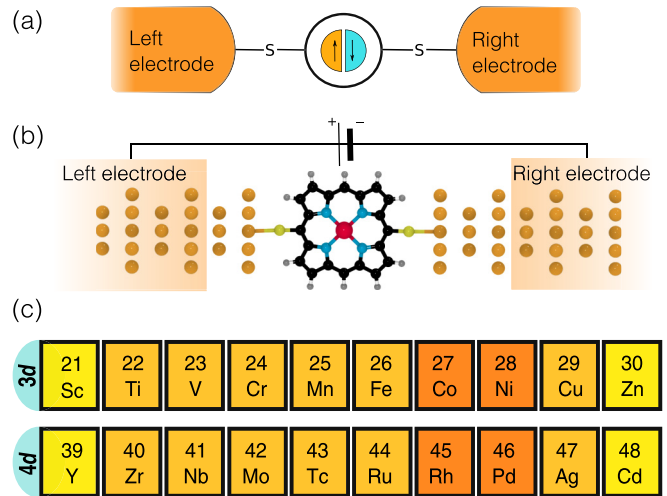

FIG. 1. (a) Structure of the investigated SMM devices, (b) Structure of *M*Por nanodevice in which *M*Por is linked to two gold electrodes via Au–S bond. The boxed regions indicated two semi-infinite gold electrodes. (c) The transition metal elements with the 3d and 4d electronic configurations are used as the inner metal for SMM devices in this work. The different colors in this table show various types of studied SMMs. The yellow, light orange, and dark orange represent the type-I, type-II′, and type-II″ spintronics, respectively.

the Au–FePor–Au device contains four Au-layer electrodes, 2 (on the left) and 3 (on the right) Au layers in extended central region connected via the S linker to *M*Por (i.e., central region) ensures the convergence of calculated transmission coefficients. So, the larger extended central region does not improve the results anymore (see Fig. S2 (SM) [46]). The lattice distance between supercell inputs in transverse direction is set as 30 Å to avoid spurious electrostatic interactions. The sulfur linker has lone electron pairs and also makes the molecular object more electron rich. Even Tivanski and co-workers [50] experimentally reported the improved conductivity with double thiol linkers compared with the single linker, but for the other molecule. Here we have used a single S for the sake of simplicity.

The *M*Por–S linker atom and S–Au electrode separations are relaxed to 1.72 and 2.23 Å, corresponding to the obtained DFT optimized bond length elsewhere [51]. $1 \times 1 \times 100$ k mesh was used to sample the first Brillouin zone along periodic direction (gold electrodes) for electrode simulations.

To consider the effect of side-chain groups on conductance properties of *M*Por devices, we compared the conductance of [4-(S-acetylthio) phenyl]-10,20-tetraphenyl (ZntpPor), [4-(S-acetylthio) phenyl]-10,20-diphenyl (ZndpPor), and ZnPor—used as scattering region in this work (Fig. S3 (SM) [46]). As seen in Table S2, the side chain has, if anything, only a negligible effect on the calculated current values, which justify the choice of *M*Por for the central region. By considering the type of inner metal ion [Fig. 1(c)], 20 devices are set up and investigated for spin-transport conductance characteristic under applied bias voltages. 5 and 100 k points are used for device and conductance calculations, respectively. A level broadening of $\eta = 10^{-6}$ eV is considered in the electrodes simulations. The energy separation for spin-
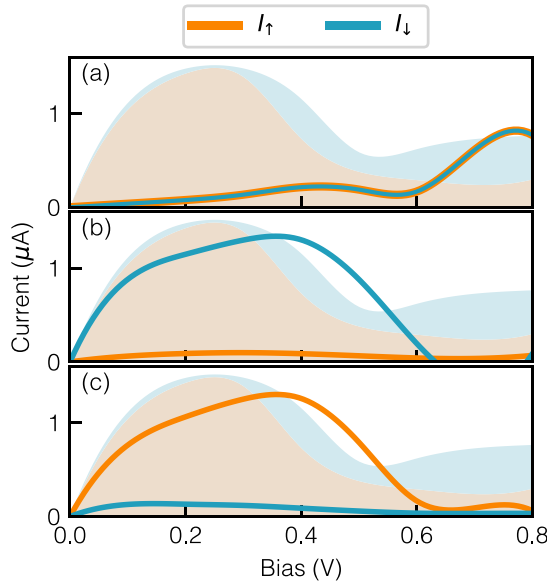
FIG. 2. Calculated spin-resolved I-V curves of (a) Au–ScPor–Au (representative of type-I devices), (b) Au–VPor–Au (representative of type-II′ spintronics), and (c) Au–CoPor–Au devices (representative of type-II″ spintronics). The orange- and blue-filled plots show the $I_\uparrow$ and $I_\downarrow$ of pristine devices.

current calculations sets as 0.001 eV. It may be worth noting that transmission in the forward and backward direction is the same because of the inversion symmetry of MPor complexes. Hence, we just considered the positive values of bias voltage in our computations.

After calculating the major (minor) spincurrent (I), we calculate spin-filtering efficiency (SFE) as

$$\text{SFE} = \frac{I_\uparrow - I_\downarrow}{I_\uparrow + I_\downarrow} \times 100. \tag{1}$$

III. RESULTS AND DISCUSSION

Classification of the MPor-based spintronics: Figures 2 and S4 represent spin current as a function of voltage for the designed Au–MPor–Au devices in which M comprises all the 3d and 4d transition metals. The pristine Por-based device (Au–Por–Au) is also calculated as the reference. Figure 2 shows two major types of I-V curves; non-spin-polarized (type I) and spin-polarized (type II) ones. Type I includes four ScPor-, ZnPor-, YPor-, and CdPor-based molecular devices whose I-V curves ($I_\uparrow$ and $I_\downarrow$) do not show any splitting between the two spin components. The rest of the molecular junctions (from the TiPor to CuPor and then from ZrPor to AgPor-based SMMs) are magnetic, belonging to type-II junctions.

As seen in the periodic table in Fig. 1(c), the observed magnetization depends on the occupation of d orbitals. Type I are found for 3d^1, 3d^{10}, 4d^1, and 4d^{10} electronic configuration of central metal ions. Owing to the nd filled electronic shell of Zn(II) (3d^{10}) and Cd(II) (4d^{10}) ions, the constructed molecular junctions are nonmagnetic (Tables S3 and S4 (SM) [46]) that agrees with previous experiment reported by Kang *et al.* [52] The delocalized nature of nd^1 electrons of Sc- and Y-based Por complexes leads to nonmagnetic molecular

junctions [40]. Since there is no spin polarization for type I (see Figs. S5, S14, S15, and S24 (SM) [46]), they are irrelevant to spintronic devices.

Metal ions with 3d^2 to 3d^9, and 4d^2 to 4d^9 electronic configurations, placed at the center of a Por ring, lead to type-II curves. All such MPors and their built junctions are magnetic or become magnetic upon voltage biasing (see Tables S3 and S4 (SM) [46]). The calculated magnetic values of type-II MPors show an excellent agreement with the previous work [28,40]. For this type, spin-polarized currents are observed (see Figs. 2 and S4). Type-II itself can be categorized into two subtypes; designated as type II′ and type II″. Type-II′ spintronics for devices with nd^2 to nd^6 and then nd^9 electronic configuration of a central ion magnet in which the minor spin component governs the output current. On the other hand, type-II″ devices are obtained for central metal ions with nd^7 and nd^8 electronic structures in which a major spin component governs the output current. In the body of the present work, the type of spin-configuration polarization for type-II′ and type-II″ systems will be express as *minor spin polarization* and *major spin polarization*. In type II′, the obtained $I_\downarrow$ (blue curve) is around 14 to 15 times more than $I_\uparrow$ (orange curve) within bias voltages from 0.1 to 0.5 V (Figs. 2(b) and S4 and Table S5 (SM) [46]). After this bias region, the calculated currents drop to almost zero for both $I_\uparrow$ and $I_\downarrow$. The type II″ resembles similar traits, where the major spin current is polarized (Figs. 2(c) and S4 and Table S5 (SM) [46]). Despite subtle differences, the quantity values of spin-polarized currents at obtained bias points are pretty similar for both subtypes. The maximum value of 1.5 μA is obtained for the spin-polarized current of type-II devices.

Transmission spectra analysis of type-I junctions: The notable change in I-V curves of non-spin-polarized compared to the pristine one can be understood by the relative energy positions of Sc, Zn, Y, and CdPor molecular orbitals to the Au states. As seen in Figs. S5, S14, S15, and S24, the transmission peaks (for major and minor spin electrons) of devices with nd^1 electronic state was placed outside the bias window at zero voltage, moving toward the bias window as the voltage increases. So the spin currents increase (Fig. S4 (SM) [46]). For the devices with nd^{10}, the transmission peaks are inside the bias window at zero voltage, and the height of the resonance peak decreases by applying voltages (Figs. S14 and S24 (SM) [46]) and the spin currents reduce.

Transmission spectra analysis of type-II spintronics: To analyze the results, we resort to transmission spectra and spatial distribution of MOs in the presence of Au electrodes (MPSH) at zero bias voltage for all 3d and 4d MPor-based devices. The transmission spectra of Au–VPor–Au and Au–CoPor–Au within the bias range of 0.0 to 0.6 V are shown in Fig. 3(a) (for more details, see Figs. S5 to S24 of the SM [46]). The sharp resonance peak at around the E_F (see Fig. 3(a) and Figs. S6 to S13 and S16 to S23 (SM) [46]) mainly contribute to spin-polarized current.

Figure 3 indicates that the conductivity of the major and minor spin channels are well separated. Minor spin electrons mainly cause a sharp resonance peak at around E_F for type-II′ molecular objects. By applying voltage, the resonance peak enters in the bias window (increasing the $I_\downarrow$) and reaches its maximum value at the bias = 0.4 V. Beyond this voltage,
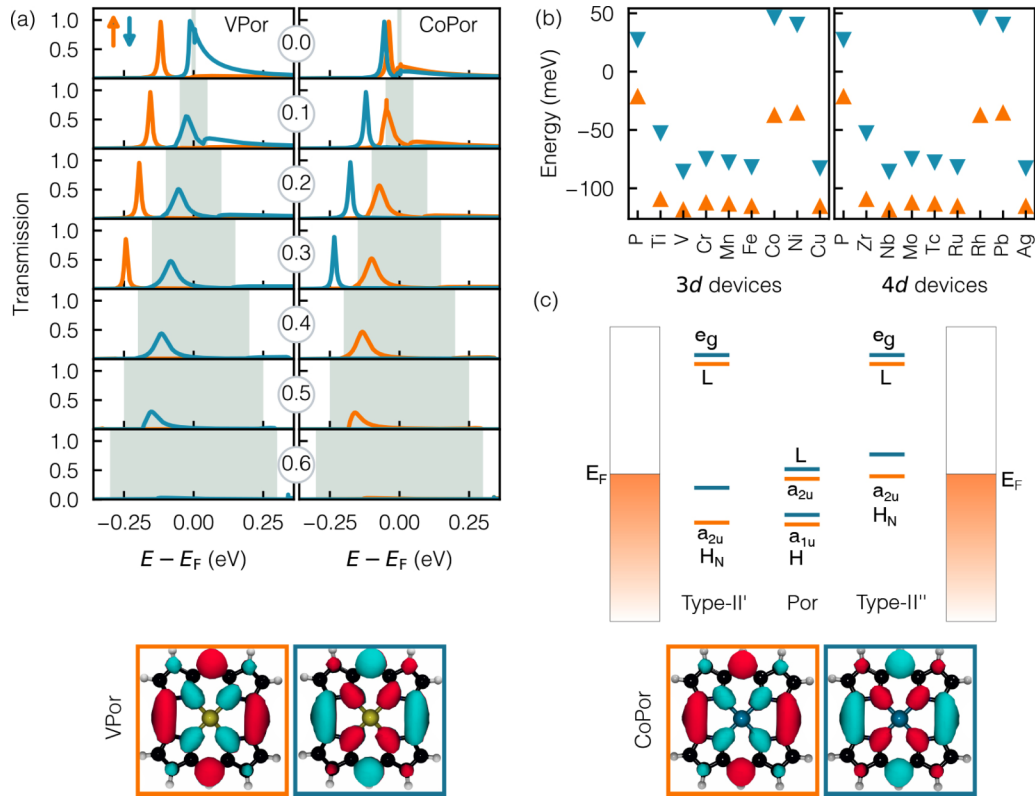
FIG. 3. (a) Spin-resolved transmission functions of Au–VPor–Au and Au–CoPor–Au junction at 0 to 0.6 bias voltage. Spatial distributions of the MPSHs are found for the Au–VPor–Au and Au–CoPor–Au junctions to lie in the relevant energy window. (b) Calculated spin-resolved energetic position of MPSH$_{\uparrow(\downarrow)}$ of $3d$- and $4d$-molecular devices at zero bias. (c) Schematic representation of the centered MPor molecular levels for type-II′ and type-II″ junctions. H and L stand for HOMO and LUMO eigenstates. The pristine device (P) molecular energy levels are given for comparison. The orange and blue colors represent the major and minor spin related information.

the resonance peak is strongly suppressed, falling to zero $I_\downarrow$ for type II′ (Figs. 2(a) and S4 (SM) [46]). The observed behavior can be attributed to the spin-dependent negative differential resistance (SNDR), commonly found in molecular junctions [3,53]. The SNDR behavior can be explained from the changes in the transmission spectrum at different applied voltages. For the minor spin channel, the overall transmission at low voltages (e.g., 0.4 V) is higher than large voltages; therefore, the integrated sum results in a higher $I_\downarrow$ at 0.4 V, giving rise to the SNDR$_\downarrow$ effect. The NDR effect that is observed in the pristine devices (Fig. 2, filled region curves) and also metal-centered ones (Figs. 2 and S4) is attributed to the coupling between the a_{2u} molecular orbital and those states of Au electrodes placed around the E_F. The strength of the coupling depends, of course, on the applied bias voltages. Long and co-workers also report such NDR mechanism for Por-based molecular junctions [54].

For the majority spin channel, the transmission coefficients are essentially zero at around the E_F for all the applied bias voltages, and the resonance peak lies far outside any reasonable bias window for major spin component. These features are the primary reason for the zero value of the $I_\uparrow$ in all the bias regions for type-II′ devices. This structure gives spin-polarized current to the type-II′ molecular objects. The transmission spectra of type II′ show no considerable deformations by the applied bias. As we can see, there is no contribution from other transmission peaks related to the

different molecular orbital in conductance path. Note that the bias voltage only shifts and widens the transmission resonance peak of type II′.

To get a deeper insight into the spin-dependent transport of the studied SMMs, we perform molecular projected self-consistent Hamiltonian (MPSH) analysis using Inelastica code [55]. The eigenstates of MPSH are associated with molecular orbitals, which are normalized by the interaction between molecule and electrode. The MPSH energy positions for type II in the presence of Au electrodes are presented in Figs. 3(b) and 3(c), and Tables S6 and S7 (SM). As discussed in the previous work [56], the energy and symmetry of molecular orbitals strongly depend on exchange fraction and the presence of self-interaction correction (SIC). The Hubbard U correction takes SIC into account [57,58] and can correct the localized nature of pure DFT methods. Thus the energetics and magnetizations improve by Hubbard U corrections providing results comparable with those of HSE calculations for solids [58] and molecules [59]. To check the dependence of the results upon the choice of functionals, we repeat some of the calculations using BLYP—a GGA functional that benefits from Becke exchange—which is known to be successful for molecular systems. The energy level calculations for VPor and CoPor (as representative of type-II′ and type-II″ spintronics) are recalculated using BLYP functionals. Tables S6 and S7 (SM) list the obtained MPSH energy levels of VPor and CoPor. As seen there, the BLYP results follow the PBE ones.

Note that the MPSH$_\uparrow$ and MPSH$_\downarrow$ for the pristine device are matched with the Por $a_{2u\uparrow}$ and $a_{2u\downarrow}$ molecular orbitals located at -21 and 27 meV to the E_F. The a_{2u} MO was reported as HOMO$_N$ of the isolated MPor complexes [60,61]. There is a strong hybridization between $a_{2u\uparrow}$ and $a_{2u\downarrow}$ of Por molecule, p orbital of S linker atoms and d bands of the Au electrodes (Figs. 3 and S25). It can be understood that the S linker atoms continue the π conjugation from the molecule into the Au electrode. Thus, π-conjugated states—delocalized over the Por ring—put up a fast channel for electron flow and enhanced transmission coefficients. Indeed, the minor spin-current transports through the π-conjugated network of the Por unit in the type-II$'$ SMMs. Based on our analysis and also the result reported by Kim and co-workers [14], other molecular orbitals—in particular, those states placed over the central M—do not contribute to electrical transmission. Only the Por's a_{2u} contributes to the transmission resonance at the bias window; Thus, a similar I-V behavior for all the type-II devices has been observed. Previous theoretical works also report a similar MO contribution [62].

For type-II$'$ devices, the MPSH$_\uparrow$ and MPSH$_\downarrow$ are positioned at around -120 and -70 meV relative to the E_F [see Fig. 3(b)]. As a result, introducing metal ion into Por ring downshifts the $a_{2u\uparrow}$ and $a_{2u\downarrow}$ MO energy levels. The calculated MPSH$_\uparrow$ and MPSH$_\downarrow$ for devices with $3d^n$ and $4d^n$ central ions (n changes equally for $3d$ and $4d$ metals) are close to one another (Table S6 (SM) [46]). However, devices with $4d$ central ions show slightly more negative energy levels with respect to the $3d$ molecular spintronics. The MPSH$_\uparrow$ is deeper than the MPSH$_\downarrow$ with respect to the E_F, as shown in Figs. 3(b) and 3(c), implying that it is much easier to provide a proper level alignment for charge transport in the case of high-lying MPSH$_\downarrow$ energy levels of MPor. This provides a perfect channel for minority electrons within the bias window. However, the majority spin channel is positioned outside of the device bias window [for the $3d$ devices, see Figs. S6 to S10 and S12, and for the $4d$ devices, see Figs. S16 to S20 and S22 (SM)]. So, the minor spin current directly transports to the other Au electrode and will cause high $I_\downarrow$ [Figs. 2(b) and S4]. The outside level does not contribute to the spin-current flow, and the type-II$'$ molecular junctions act as a one-level system with a *selective* inflow of minor spin current. The type-II$'$ molecular junctions are half-metals, which are conducting for minor spin direction and insulating for the opposite direction [63]. The type-II$'$ devices can work as an ideal ferromagnet for major spin-component filtering and sources of minor spin-polarized current. However, the inner metal ion has no special effect on the type-II$'$ conductance trends. It is responsible for the modification of MPSH$_{\uparrow\downarrow}$ energy positions close to the E_F, resulting in spin-polarized conductance.

The MPSH analysis can also explain the abrupt switching of device spin polarization between II$'$ and II$''$ systems. The type-II$''$ MPSH$_\uparrow$ intersects the E_F and thus their conductance is dominated by majority spins [see Fig. 3(a) and Figs. S11, S12, S21, and S22]. Compared with the pristine device and type-II$'$ counterpart, incorporating a metal core can lead to an up-shift of the MPSH energy levels and lower stability. For the type-II$''$ devices the $a_{2u\uparrow}$ and $a_{2u\downarrow}$ are the HOMO and LUMO$_N$ of the molecular objects. The choice of central metal in MPor affects the MPSH energy levels referenced to

pristine—without M—devices. Such metal-dependent spin-tronic feature bestows MPor various functionalities such as spin filtering and spin switchability, which will be discussed in the following.

For type-II$''$ nanodevices, the major spin current rises linearly with the increasing of the applied bias when the voltage is less than 0.4 V. Then it drops down to almost zero at high voltages. From Fig. 3(a) it is clear the transmission peaks for both spin components widen gradually under the influence of level broadening, as what we observed for the type II$'$. The width of the transmission resonance peak depends on molecule-electrode coupling strength at various bias voltages. As the bias voltage increases, the height of resonance peak decreases, indicating that the coupling between states of a molecule and left/right Au electrodes decreases [64]. Therefore, the spin-negative differential resistance for major spin current can be observed in the type-II$''$ systems. As already discussed, type II$'$ has shown minor spin NDR while the type-II$''$ junctions have demonstrated major spin NDR effect. The low-bias spin-splitted NDR is a very interesting functional to reduce power consumption of spintronics, which can be widely applied for spintronic fabrications such as memories, tunnel diodes, mixers, fast switches, etc. [62,65–67]. The MPSH$_\downarrow$ lies far outside of any reasonable bias window for type II$''$. So, there is a zero $I_\downarrow$ in all biases. The obtained I-V trend is similar to the type-II$'$, but the current is just polarized for the major spin component. This happens because of the spin-electrons transport through the π-conjugated network of the MPSH$_\uparrow$. Then, for both type-II$'$ and type-II$''$ molecular objects, the minor and major spin currents flow in the same MO with π-delocalized nature (a_{2u}), resulting in similar values of spin current for both investigated devices (see Figs. 2 and S4). For type-II$''$ spintronics, the minority spin channel is located outside the bias window [see Figs. 3(a) and S11, S12, S21, and S22]. Consequently, just the $I_\uparrow$ can transport into the device, leading to the spin polarization for major spin components. Such devices work as a one-level system with selective conductance of major spin current. The type-II$''$ molecular junctions are half-metals, which are conducting for major spin direction and insulating for the opposite direction.

Depending on the electronic configuration of the central ion magnet, MPor can conduct for the majority or minority spin electrons. So, type-II$'$ systems are majority spin filters while type-II$''$ systems are minority spin filters. It can be concluded that the spin-polarized transport behavior of type-II devices originates from the energetic position of the $a_{2u\uparrow(\downarrow)}$ with respect to the bias window [Figs. 3(a) and 3(c)] caused by the presence of both paramagnetic and diamagnetic metal ion (Tables S3 and S4 (SM) [46]) at the center of each porphyrin moiety. This implies that the spin filtering for the Au–MPor–Au systems is an inherent trait of the MPors and not the device. This is a significant result as it shows the viability of the molecular approach to spintronics.

Spin magnetic moment switching of type-II$''$ spintronics: The spin magnetic moment (μ_s) values of the Au–MPor–Au molecular junctions at different bias voltages using PBE functional are shown in Tables S3 and S4 (SM). The PBE functional might underestimate magnetic moment because of its delocalized nature. However, Hubbard U should solve, at least in part, this problem. Sun *et al.* [6] show that GGA+U

TABLE I. Calculated Mulliken spin moment (μ_s) values of the Co and Ni molecular junctions at different bias voltages. The spin moments are provided for the inner-metal, Por ring, and S linker atoms, separately.

Device	TM	0.0	0.1	0.2	0.3	0.4	0.5	0.6	0.7	0.8
Au–CoPor–Au	Co	1.47	1.47	1.42	1.14	1.14	1.13	1.15	1.14	1.15
	Por	−0.19	−0.23	−0.40	−0.04	−0.37	−0.49	−0.52	−0.51	−0.51
	S	−0.14	−0.18	−0.23	−0.27	−0.29	−0.34	−0.37	−0.39	−0.36
Au–NiPor–Au	Ni	0.00	0.00	0.00	0.00	0.00	0.00	0.00	0.00	0.00
	Por	−0.17	−0.20	−0.29	−0.28	−0.30	−0.18	−0.32	−0.43	−0.27
	S	−0.15	−0.19	−0.27	−0.27	−0.30	−0.34	−0.37	−0.37	−0.35

correctly calculate μ_s and the switching behavior of Mn-phthalocyanine, giving comparable results to those of hybrid functionals such as HSE, B3LYP, and PBE0. We have also calculated the μ_s of VPor- and CoPor-based devices as representative of type-II′ and type-II″ devices using BLYP. The estimated μ_s values calculated by BLYP are in acceptable agreement with those of BPE functional, whereby μ_s monotonically decreases for Au–CoPor–Au.

As expected for an SMM, the unpaired nd electrons in a transition-metal atom can induce a proper magnetic moment value into the MPor devices. The magnetic moment reaches the maximum value of 5 μ_B in MnPor, complying with the tendency of Mn complexes to form a high-spin state [68]. Except for Co-, Ni-, Rh-, and Pd-based molecular junctions, the μ_s show no monotonic increase or decrease under applied bias voltages. Spin population analysis shows that the device spin magnetic moment is concentrated on the cobalt atom with d^7 electronic configuration at equilibrium state (Table I and Fig. 4).
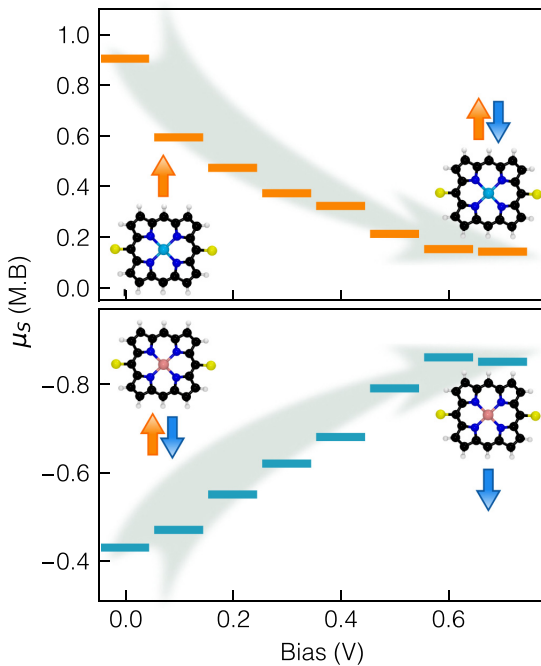

FIG. 4. Calculated spin magnetic moment values of Au–CoPor–Au (top) and Au–NiPor–Au (bottom) junctions at different bias voltages. The figures exhibit transition between different spin states for type-II″ devices.

In the nonequilibrium state, the population analysis shows that the minor spin density spreads over the Por ring and sulfur atoms. In contrast, the spin population of central metal ion remains unchanged (Table I). The spin magnetic moment on the Por and S atoms increases to the values corresponding to −0.51 and −0.36 μ_B at bias = 0.8 V, coupled antiferromagnetically to the central cobalt atom. The monotonic decreasing of the spin moment for Au–CoPor–Au is also achieved using PBE functional (see Table S8 of the SM). The NiPor and PdPor are diamagnetic as expected from their d^8 electron configuration at the square planar structure [69]. In the nonequilibrium state, we observe that the Por ring and the S-linker atoms possess an induced magnetic moment of −0.27 and −0.35 μ_B at bias = 0.8 V, respectively.

The presence of spin electron on the S-linker atoms is because the E_F lies in the central molecule HOMO–LUMO gap [70] for type II″. Thus, the CoPor and RhPor junctions undergo switching from a medium spin state (doublet) to a low spin state (singlet) upon voltage biasing. On the contrary, NiPor and PdPor systems undergo switching from a low spin state (singlet) to a medium spin state (doublet) upon voltage biasing (see Fig. 4). The spin transition for the devices is obtained at low voltages, a property that can be used for memory applications in spintronics fabrication [71,72].

Spin filtering efficiency of type-II spintronics: Equation (1) can approximate the spin polarization at different voltages. The calculated SFE for different voltages has been mapped onto the colored plots in Fig. 5. The approximate SFE values for type-II′ devices are obtained around −90% within voltages from 0.2 to 0.4 V, showing their half-metallic nature. The higher SFE values around −95% for major spin filtering are obtained for devices with Cr and Fe central ions at voltages around 0.2 to 0.4 V. A negative value of SFE shows that the contribution of the minor spin components is higher than the major spin components. The type-II″ systems function with the same efficiency (around 90%) observed at bias = 0.2 to 0.4 V but as minor spin filters. We should emphasize that in type-II devices, spin polarization is almost independent of applied voltages within the range of 0.0–0.4 V, indicating that SFE remains intact.

These results indicate that the SFE characteristics in the type-II systems can be obtained at the specified voltages. However, this feature is not seen in the pristine device (see Figs. 2 and S4). It suggests that the SFE of type-II junctions arises because of the inner magnetic ions. For our designed devices, low voltages may lead to highly polarized spin currents which are of technological interest [73,74]. All the results mentioned above demonstrate the rational choices of a single
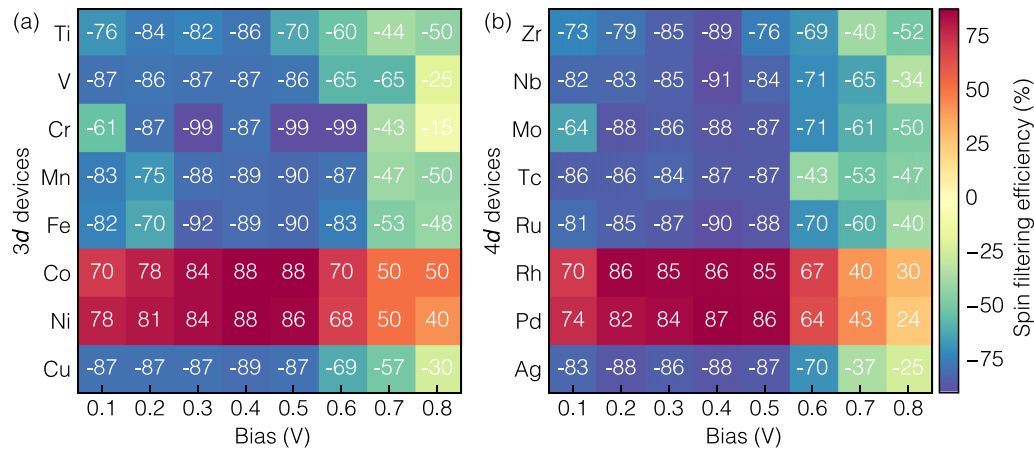
FIG. 5. Calculated spin filtering efficiency as function of voltage for (a) 3d-molecular devices and (b) 4d-molecular devices.

atom can lead to the unique system's spintronic behavior and lead to new functions for SMMs such as spin switching and spin filtering. In practical applications, more extensive computational simulations need to be carried out. For example, it would be interesting to simulate the spintronic conductance behavior of MPors adsorbed on a metal surface, the effect of spin-spin correlation in the dimer, trimer, and polymer of MPor compounds, and analysis of the MPors molecular junctions as the gas sensors. We may note that different Au-layer stacking and a fully bulk electrode may provide different absolute conductance values, though the trend of conductance should still be the same. The dependence of MPors spintronic behavior to the nature of the electrodes could be further studied to determine whether electrodes play a major role in spintronic of device or not.

IV. CONCLUSIONS

In summary, we have studied the spin-transport properties of metalloporphyrin molecules, including all the 3d and 4d metals centers. Except for the Sc-, Zn-, Y-, and Cd-based molecular junctions, we find spin-polarized transport behavior for all investigated junctions. An abrupt switching in spin-polarized current from minor to significant spin component is observed for the Co, Ni, Rh, and Pd devices. MPSH analysis reveals that spin switching is rooted in the energy-level position of the MPor molecular orbitals. For the type-II″ junctions, the E_F is between the MPSH$_\uparrow$ and MPSH$_\downarrow$, while for the type-II′ systems, they are placed deeper in energy relative to E_F. The energy-dependent alignment of MO and Au electrode bands provides a unique pattern for the type-II′

and type-II″ junctions; just one spin path (minor or major) can enter the bias window. The type-II systems perform as a one-channel transport device, resulting in half-metallic nature and spin filtering efficiency. We find all devices exhibit nonlinear molecular transport behavior upon voltage biasing. The spin-current switching from low-to-high and then high-to-low for minor and major spin-polarized current of type-II′ and type-II″ systems is realized SNDR$_\downarrow$ and SNDR$_\uparrow$ property to our devices. We should conclude that for Co-, Ni-, Rh-, and Pd-based SMMs, there is a spin-state switchability at a low studied bias region. We find that MPor molecular magnets establish a very promising playground for the design of advanced molecular spintronics such as major (type-II″) and minor (type-II′) spin filter, memory (type II″), etc. Though former studies have proposed novel spintronic devices, none of them are realized because of the lack of practical fabrication methods in experiments. However, a spintronic device based on MPors offers a synthesizable framework that can be achieved experimentally.

[1] M. Mannini, F. Pineider, P. Sainctavit, C. Danieli, E. Otero, C. Sciancalepore, A. M. Talarico, M.-A. Arrio, A. Cornia, D. Gatteschi *et al.*, Nat. Mater. **8**, 194 (2009).

[2] G. Avvisati, P. Gargiani, C. Mariani, and M. G. Betti, Nano Lett. **21**, 666 (2021).

[3] D. Wu, X.-H. Cao, S.-Z. Chen, L.-M. Tang, Y.-X. Feng, K.-Q. Chen, and W.-X. Zhou, J. Mater. Chem. A **7**, 19037 (2019).

[4] T. Jasper-Toennies, M. Gruber, S. Karan, H. Jacob, F. Tuczek, and R. Berndt, Nano Lett. **17**, 6613 (2017).

[5] A. N. Pal, D. Li, S. Sarkar, S. Chakrabarti, A. Vilan, L. Kronik, A. Smogunov, and O. Tal, Nat. Commun. **10**, 1 (2019).

[6] M. Sun, X. Wang, and W. Mi, J. Chem. Phys. **147**, 114702 (2017).

[7] A. Cornia and P. Seneor, Nat. Mater. **16**, 505 (2017).

[8] L. Garnier, B. Verlhac, P. Abufager, N. Lorente, M. Ormaza, and L. Limot, Nano Lett. **20**, 8193 (2020).

[9] P. Sessi, T. Bathon, K. Kokh, O. E. Tereshchenko, and M. Bode, Nano Lett. **14**, 5092 (2014).

[10] M. N. Leuenberger and D. Loss, Nature (London) **410**, 789 (2001).

[11] Y. Li, K. Xu, and X. Sun, Instrum. Sci. Technol. **48**, 518 (2020).

[12] N. Xin, J. Guan, C. Zhou, X. Chen, C. Gu, Y. Li, M. A. Ratner, A. Nitzan, J. F. Stoddart, and X. Guo, Nat. Rev. Phys. **1**, 211 (2019).

[13] G. Kuang, Q. Zhang, T. Lin, R. Pang, H. Shi, H. Xu, and N. Lin, ACS Nano **11**, 6295 (2017).

[14] W. J. Cho, Y. Cho, S. K. Min, W. Y. Kim, and K. S. Kim, J. Am. Chem. Soc. **133**, 9364 (2011).

[15] Q. Sun, L. M. Mateo, R. Robles, P. Ruffieux, N. Lorente, G. Bottari, T. Torres, and R. Fasel, J. Am. Chem. Soc. **142**, 18109 (2020).

[16] A. Ostovan, N. Papior, M. Zahedi, and A. Z. Moshfegh, Phys. Chem. Chem. Phys. **22**, 23128 (2020).

[17] G. Liu, H. Cui, S. Wang, L. Zhang, and C.-Y. Su, J. Mater. Chem. A **8**, 8376 (2020).

[18] D. Zhu, M. Qiao, J. Liu, T. Tao, and C. Guo, J. Mater. Chem. A **8**, 8143 (2020).

[19] S. Arrechea, A. Aljarilla, P. de la Cruz, E. Palomares, G. D. Sharma, and F. Langa, Nanoscale **8**, 17953 (2016).

[20] Y.-C. Liu, H.-H. Chou, F.-Y. Ho, H.-J. Wei, T.-C. Wei, and C.-Y. Yeh, J. Mater. Chem. A **4**, 11878 (2016).

[21] J. P. Perdew, K. Burke, and M. Ernzerhof, Phys. Rev. Lett. **77**, 3865 (1996).

[22] J. M. Soler, E. Artacho, J. D. Gale, A. García, J. Junquera, P. Ordejón, and D. Sánchez-Portal, J. Condens. Matter Phys. **14**, 2745 (2002).

[23] N. Troullier and J. Martins, Solid State Commun. **74**, 613 (1990).

[24] V. I. Anisimov, F. Aryasetiawan, and A. I. Lichtenstein, J. Phys. Condens. Matter **9**, 767 (1997).

[25] A. Jain, G. Hautier, S. P. Ong, C. J. Moore, C. C. Fischer, K. A. Persson, and G. Ceder, Phys. Rev. B **84**, 045115 (2011).

[26] S. Kirklin, J. E. Saal, B. Meredig, A. Thompson, J. W. Doak, M. Aykol, S. Rühl, and C. Wolverton, npj Comput. Mater. **1**, 15010 (2015).

[27] L. J. Boucher, J. Am. Chem. Soc. **92**, 2725 (1970).

[28] C. Wäckerlin, K. Tarafder, D. Siewert, J. Girovsky, T. Hählen, C. Iacovita, A. Kleibert, F. Nolting, T. A. Jung, P. M. Oppeneer *et al.*, Chem. Sci. **3**, 3154 (2012).

[29] I. Morishima, Y. Shiro, and K. Nakajima, Biochemistry **25**, 3576 (1986).

[30] P. M. Oppeneer, P. M. Panchmatia, B. Sanyal, O. Eriksson, and M. E. Ali, Prog. Surf. Sci **84**, 18 (2009).

[31] N. Chizhova, O. Maltceva, S. Zvezdina, N. Z. Mamardashvili, and O. Koifman, Russ. J. Gen. Chem. **88**, 978 (2018).

[32] Z.-Y. Wu, T. Wang, Y.-S. Meng, Y. Rao, B.-W. Wang, J. Zheng, S. Gao, and J.-L. Zhang, Chem. Sci. **8**, 5953 (2017).

[33] G. M. Godziela and H. M. Goff, J. Am. Chem. Soc. **108**, 2237 (1986).

[34] C. Mchiri, S. Dhifaoui, K. Ezzayani, M. Guergueb, T. Roisnel, F. Loiseau, and H. Nasri, Polyhedron **171**, 10 (2019).

[35] P. M. Panchmatia, B. Sanyal, and P. M. Oppeneer, Chem. Phys. **343**, 47 (2008).

[36] H. K. Singh, P. Kumar, and U. V. Waghmare, J. Phys. Chem. C **119**, 25657 (2015).

[37] J.-J. Zheng, Q.-Z. Li, J.-S. Dang, W.-W. Wang, and X. Zhao, AIP Adv. **6**, 015216 (2016).

[38] M. E. Ali, B. Sanyal, and P. M. Oppeneer, J. Phys. Chem. C **113**, 14381 (2009).

[39] S. Doble, A. J. Osinski, S. M. Holland, J. M. Fisher, G. R. Geier III, R. V. Belosludov, C. J. Ziegler, and V. N. Nemykin, J. Phys. Chem. A **121**, 3689 (2017).

[40] P. Kratzer, S. A. Tawfik, X. Y. Cui, and C. Stampfl, RSC Adv. **7**, 29112 (2017).

[41] H. Ammar and H. Badran, Heliyon **5**, e02545 (2019).

[42] A. R. Groenhof, M. Swart, A. W. Ehlers, and K. Lammertsma, J. Phys. Chem. A **109**, 3411 (2005).

[43] W. Wang, R. Pang, G. Kuang, X. Shi, X. Shang, P. N. Liu, and N. Lin, Phys. Rev. B **91**, 045440 (2015).

[44] M. Dommaschk, J. Gröbner, V. Wellm, J.-B. Hövener, C. Riedel, and R. Herges, Phys. Chem. Chem. Phys. **21**, 24296 (2019).

[45] R. Li, Z. Feng, Y. Li, X. Dai, Y. Ma, and Y. Tang, Appl. Surf. Sci. **520**, 146202 (2020).

[46] See Supplemental Material at http://link.aps.org/supplemental/10.1103/PhysRevB.104.235435 for the details on simulation models and procedure, calculations of spin magnetic moment, spin current, and spin transmission of all 3d and 4d metal-ions junctions at 0 to 0.8 bias voltages; spatial distributions of the MPSHs for type-II devices.

[47] N. Papior, N. Lorente, T. Frederiksen, A. García, and M. Brandbyge, Comput. Phys. Commun. **212**, 8 (2017).

[48] W. Ding, M. Koepf, C. Koenigsmann, A. Batra, L. Venkataraman, C. F. Negre, G. W. Brudvig, R. H. Crabtree, C. A. Schmuttenmaer, and V. S. Batista, J. Chem. Theory Comput. **11**, 5888 (2015).

[49] Y. Li, M. Hodak, W. Lu, and J. Bernholc, Carbon **101**, 177 (2016).

[50] A. V. Tivanski, Y. He, E. Borguet, H. Liu, G. C. Walker, and D. H. Waldeck, J. Phys. Chem. B **109**, 5398 (2005).

[51] W. Ding, C. F. Negre, L. Vogt, and V. S. Batista, J. Chem. Theory Comput. **10**, 3393 (2014).

[52] B. K. Kang, N. Aratani, J. K. Lim, D. Kim, A. Osuka, and K.-H. Yoo, Chem. Phys. Lett. **412**, 303 (2005).

[53] A. Ostovan, Z. Mahdavifar, and M. Bamdad, J. Mol. Liq. **269**, 639 (2018).

[54] M.-Q. Long, K.-Q. Chen, L. Wang, W. Qing, B. Zou, and Z. Shuai, Appl. Phys. Lett. **92**, 243303 (2008).

[55] T. Frederiksen, M. Paulsson, M. Brandbyge, and A.-P. Jauho, Phys. Rev. B **75**, 205413 (2007).

[56] D. A. Egger, S. Weissman, S. Refaely-Abramson, S. Sharifzadeh, M. Dauth, R. Baer, S. Kummel, J. B. Neaton, E. Zojer, and L. Kronik, J. Chem. Theory Comput. **10**, 1934 (2014).

[57] T. Tsuneda and K. Hirao, J. Chem. Phys. **140**, 18A513 (2014).

[58] A. Janotti and C. G. Van de Walle, Phys. Status Solidi B **248**, 799 (2010).

[59] X. Sun, Z. Y. Li, M. Jibran, A. Pratt, Y. Yamauchi, and B. Wang, Phys. Chem. Chem. Phys. **19**, 32655 (2017).

[60] M.-S. Liao and S. Scheiner, J. Chem. Phys. **117**, 205 (2002).

[61] T. Vangberg, R. Lie, and A. Ghosh, J. Am. Chem. Soc. **124**, 8122 (2002).

[62] K.-H. Kim, H.-Y. Park, J. Shim, G. Shin, M. Andreev, J. Koo, G. Yoo, K. Jung, K. Heo, Y. Lee *et al.*, Nanoscale Horiz. **5**, 654 (2020).

[63] J. Deng, N. Liu, J. Guo, and X. Chen, Phys. Rev. B **99**, 184409 (2019).

[64] Z.-F. Liu and J. B. Neaton, J. Phys. Chem. C **121**, 21136 (2017).

[65] S. V. Inge, N. K. Jaiswal, and P. N. Kondekar, Adv. Mater. Interfaces **4**, 1700400 (2017).

[66] P. K. Srivastava, Y. Hassan, D. J. de Sousa, Y. Gebredingle, M. Joe, F. Ali, Y. Zheng, W. J. Yoo, S. Ghosh, J. T. Teherani *et al.*, Nat. Electron **4**, 269 (2021).

[67] Y. Yamazaki, K.-i. Yamashita, Y. Tani, T. Aoyama, and T. Ogawa, J. Mater. Chem. C **8**, 14423 (2020).

[68] X. Huang, T. Zhuang, P. A. Kates, H. Gao, X. Chen, and J. T. Groves, J. Am. Chem. Soc. **139**, 15407 (2017).

[69] V. Bachler, G. Olbrich, F. Neese, and K. Wieghardt, Inorg. Chem. **41**, 4179 (2002).

[70] A. R. Rocha, V. M. Garcia-Suarez, S. W. Bailey, C. J. Lambert, J. Ferrer, and S. Sanvito, Nat. Mater. **4**, 335 (2005).

[71] M. Zeng, W. Huang, and G. Liang, Nanoscale **5**, 200 (2013).

[72] Q. Wu, S. Hou, H. Sadeghi, and C. J. Lambert, Nanoscale **10**, 6524 (2018).

[73] T. Chen, W. Ding, H. Li, and G. Zhou, J. Mater. Chem. C **9**, 3652 (2021).

[74] S. Ghasemi and K. Moth-Poulsen, Nanoscale **13**, 659 (2021).